CONDENSED MATTER PHYSICS

Kondo physics in antiferromagnetic Weyl semimetal $Mn_{3+x}Sn_{1-x}$ films

Durga Khadka[1]*, T. R. Thapaliya[1]*, Sebastian Hurtado Parra[2], Xingyue Han[2], Jiajia Wen[3], Ryan F. Need[4,5], Pravin Khanal[6], Weigang Wang[6], Jiadong Zang[7,8], James M. Kikkawa[2], Liang Wu[2], S. X. Huang[1†]

Topology and strong electron correlations are crucial ingredients in emerging quantum materials, yet their intersection in experimental systems has been relatively limited to date. Strongly correlated Weyl semimetals, particularly when magnetism is incorporated, offer a unique and fertile platform to explore emergent phenomena in novel topological matter and topological spintronics. The antiferromagnetic Weyl semimetal Mn_3Sn exhibits many exotic physical properties such as a large spontaneous Hall effect and has recently attracted intense interest. In this work, we report synthesis of epitaxial $Mn_{3+x}Sn_{1-x}$ films with greatly extended compositional range in comparison with that of bulk samples. As Sn atoms are replaced by magnetic Mn atoms, the Kondo effect, which is a celebrated example of strong correlations, emerges, develops coherence, and induces a hybridization energy gap. The magnetic doping and gap opening lead to rich extraordinary properties, as exemplified by the prominent DC Hall effects and resonance-enhanced terahertz Faraday rotation.

INTRODUCTION

Band structure topology is becoming an increasingly important aspect in materials research and design and is responsible for many of the exotic behaviors found in quantum materials such as strongly correlated two-dimensional (2D) electron systems (*1*), graphene (*2*), and topological insulators (*3*). More recently, band structure topology has been critical to the understanding and development of gapless topological semimetals (*4*–*6*), including Weyl semimetals (WSMs), Dirac semimetals, and nodal line semimetals. In WSMs, the conduction and valence bands cross at certain points in momentum (k–) space known as Weyl nodes (*6*). Weyl nodes appear in nondegenerate pairs with opposite chirality and act as monopoles of Berry curvature (i.e., sources or sinks of Berry flux). The spacing of the Weyl nodes in k-space is determined by the crystal and/or magnetic structure that break inversion or time-reversal symmetry and, in turn, dictates the magnitude of the intrinsic anomalous Hall effect (*7*, *8*).

While much of the work on WSMs to date has focused on weakly interacting systems, there is a growing need to address and include the effects of strong electron correlations (*9*–*12*). A classic example of strongly correlated behavior is the Kondo effect (*13*), which originates from the coupling between the spins of conduction electrons and local magnetic moments. As local magnetic moments form a lattice, the Kondo effect develops coherence and leads to the Kondo insulator (*14*, *15*). Inclusion of topological order in Kondo insulators leads to topological Kondo insulators, among which SmB_6 is an example that has attracted substantial attention (*16*). Recently, there have been increased theoretical efforts (*17*–*19*) to address the Kondo effect in WSMs and, particularly, the emergence of a Weyl-Kondo semimetal in nonmagnetic $Ce_3Bi_4Pd_3$ bulk samples (*20*). Unusual properties such as giant spontaneous Hall effect were predicted (*21*). These works suggest that strongly correlated WSMs are a fertile platform to explore new quantum phases, resulting from the interplay between Weyl and Kondo physics.

A promising material in which to study both Weyl and Kondo physics is the antiferromagnetic (AFM) WSM Mn_3Sn (*22*–*25*). Mn_3Sn has a hexagonal structure with lattice constants a = 5.67 Å and c = 4.53 Å (Fig. 1A), with a Néel temperature (T_N) of 420 K (*25*). The Mn atoms form a 2D Kagome lattice on the (0001) plane (i.e., *ab* plane) with Sn atoms sitting at the hexagon centers (Fig. 1B). Two neighboring Kagome Mn_3Sn layers are stacked along the c axis with an in-plane lattice offset (Fig. 1A). The Mn moments (~3 μ_B/Mn) form various noncollinear spin orders at different temperatures,

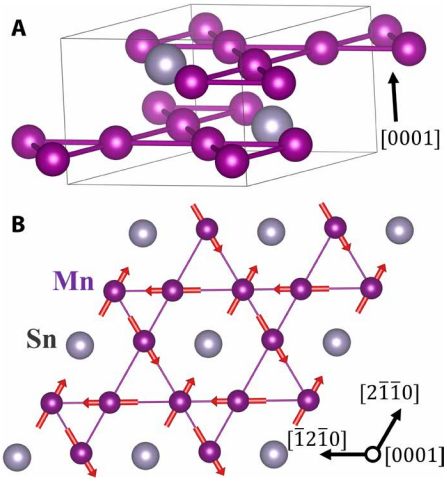

Fig. 1. Crystal structure and spin structure of Mn_3Sn. (**A**) Crystal structure of Mn_3Sn, which consists of stacked Kagome Mn_3Sn layers, and (**B**) triangular spin structure in the Kagome layer (*ab* plane).

[1]Department of Physics, University of Miami, Coral Gables, FL 33146, USA. [2]Department of Physics and Astronomy, The University of Pennsylvania, Philadelphia, PA 19104, USA. [3]Stanford Institute for Materials and Energy Sciences, SLAC National Accelerator Laboratory, Menlo Park, CA 94025, USA. [4]Department of Materials Science and Engineering, University of Florida, Gainesville, FL 32611, USA. [5]NIST Center for Neutron Research, National Institute of Standards and Technology, Gaithersburg, MD 20878, USA. [6]Department of Physics, University of Arizona, Tucson, AZ 85721, USA. [7]Department of Physics and Astronomy, University of New Hampshire, Durham, NH 03824, USA. [8]Materials Science Program, University of New Hampshire, Durham, NH 03824, USA.
*These authors contributed equally to this work.
†Corresponding author. Email: sxhuang@miami.edu

including inverted triangular structures, spin spiral, and spin glass (fig. S1 and note S1) (*26*). The most interesting are the inverted triangular spin textures (Fig. 1B) with nearly zero spontaneous magnetization (~3 × 10^{-3} μ_B/Mn). The magnetic symmetry of the inverted triangular spin textures includes mirror symmetry that ensures the appearance of the pairs of Weyl nodes at a *k* line along the local easy axis in the *ab* plane, as demonstrated by the angle-resolved photoemission spectroscopy (ARPES) measurements (*22*). The Berry curvature induced by the Weyl nodes generates a large anisotropic anomalous Hall effect (*22*, *25*). Under an external field, tilting of the triangular spin textures results in noncoplanar spin structures and generates a topological Hall effect arising from the spin Berry curvature in real space (*27*). Moreover, novel magnetic spin Hall and inverse spin Hall effects, which demonstrate field-controllable conversion between spin current and charge current, have been discovered (*24*). In addition to these unusual topological and spintronic properties, substantial bandwidth renormalization is observed because of strong correlations among Mn 3*d* electrons (*22*). These outstanding topological/spintronic properties and strong electron correlations make Mn_3Sn an ideal platform to explore the multifaceted physics of the interplay between topology, magnetism, and strong correlations, as well as the emerging topological AFM spintronics (*28*, *29*) in which thin films play a crucial role.

Here, we report the fabrication of high-quality epitaxial films of $Mn_{3+x}Sn_{1-x}$ with greatly extended compositional range (*x* up to ~0.55). We observe the Kondo effect in films with excess Mn, which substitutes for Sn and acts as a magnetic dopant in the system. Upon increased Mn doping, the system develops Kondo coherence and opens a hybridization gap. Films with $x > 0.4$ behave like Kondo insulators with topological features, as manifested in the DC Hall and terahertz Faraday rotation measurements.

RESULTS

Fabrication of epitaxial $Mn_{3+x}Sn_{1-x}$ films with greatly extended compositional range

Mn_3Sn has layered Kagome planes and exhibits a strongly anisotropic Hall effect. Thus, it is important to realize epitaxial films with two different orientations: (0001) films where the Kagome plane is in the plane of the film, and (11$\bar{2}$0) films where the Kagome plane is perpendicular to the plane of the film. There are some reports on the fabrication of near-stoichiometric Mn_3Sn films, including (0001) Mn_3Sn films on Ru seed layer (*30*), (0001) and (11$\bar{2}$0) Mn_3Sn films on MgO and Al_2O_3 substrates (*31*), and polycrystalline films on Si/SiO_2 substrate (*32*). In this work, we used cosputtering of Mn and Sn targets and realized epitaxial growth of (0001) and (11$\bar{2}$0) $Mn_{3+x}Sn_{1-x}$ films (see Materials and Methods).

We took advantage of the small lattice mismatch (~2%) between Pt (111) (cubic, $\sqrt{2}a$ = 5.55 Å) and (0001) Mn_3Sn (a = 5.67 Å), and fabricated high-quality epitaxial (0001) $Mn_{3+x}Sn_{1-x}$ films on a Pt seed layer, which is grown on C-Al_2O_3 substrate via magnetron sputtering. The θ/2θ x-ray diffraction (XRD) pattern (Fig. 2A) shows a strong

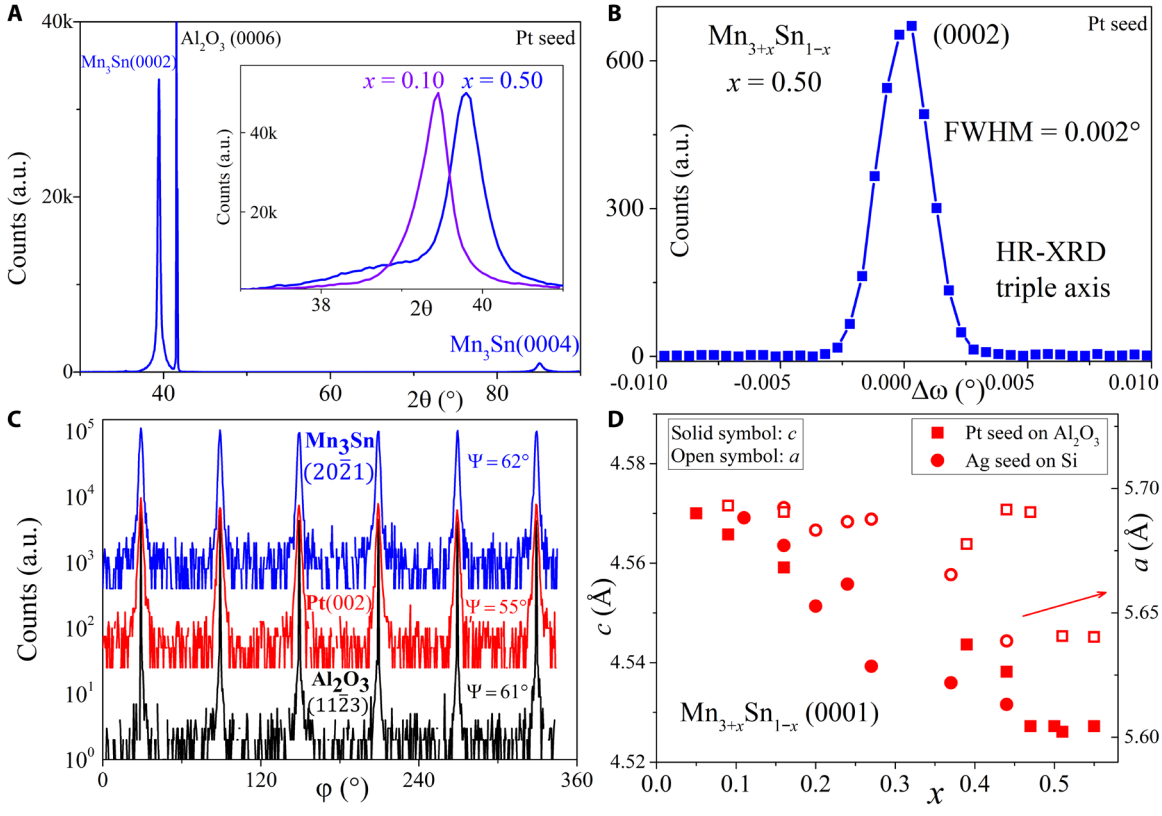

Fig. 2. Structure characterization and extended compositional range of (0001) films. (**A**) Representative XRD 2θ scan of (0001) Mn_3Sn films. Inset: XRD 2θ scan of (0001) films with different compositions. (**B**) Triple-axis high-resolution XRD (HR-XRD) ω scan (rocking curve) of $Mn_{3+x}Sn_{1-x}$ (0002) peak (x = 0.50). (**C**) In-plane φ scans of Mn_3Sn (20$\bar{2}$1), Pt (002), and Al_2O_3 (11$\bar{2}$3) planes with tilt angles Ψ are shown in the figure. (**D**) Lattice constants c (solid symbols) and a (open symbols) as a function of compositions. a.u., arbitrary units.

(0002) Mn_3Sn peak without any noticeable impurity peaks. High-resolution XRD (HR-XRD) rocking curves, collected with monochromating incident optics and a triple-axis analyzer, show a very sharp peak with full width at half maximum (FWHM) of 0.002° (Fig. 2B, for $x = 0.5$), indicating that the film has exquisite planar alignment between the (0001) crystalline plane and the film plane. Rocking curves with a double-axis analyzer showed a sharp peak with a slightly larger FWHM of 0.07° (fig. S2A), indicating a small *d*-spacing spread. For Sn-rich samples (e.g., $x = 0.1$), crystalline quality decreases slightly with a rocking curve FWHM of 0.21° (double axis, fig. S2B) and in-plane φ scan FWHM of 0.8° (fig. S2C). In-plane φ scans (Fig. 2C) of Mn_3Sn, Pt, and Al_2O_3 show six diffraction peaks, confirming the epitaxial relation of Al_2O_3 $[10\bar{1}0]$ || Pt [110] || Mn_3Sn $[2\bar{1}\bar{1}0]$. Moreover, atomic force microscopy measurements indicate that the root mean square value of the surface roughness (fig. S2D) is only about 0.4 nm. The flat surface and sharp interface between Pt and (0001) Mn_3Sn are further confirmed by x-ray reflectivity measurements (fig. S2E). We attribute the high quality of Mn_3Sn to the high-quality Pt seed layer as indicated by the Laue oscillations of the XRD Pt (111) peak (inset of fig. S2E). We note that the flat surface of (0001) Mn_3Sn is critical for future work attempting to interface Mn_3Sn with other quantum materials. Toward that end, we also grew (0001) Mn_3Sn on the integrated circuit (IC) technology–compatible substrate Si(111) with a Ag(111) seed layer (fig. S2F) and $(11\bar{2}0)$ Mn_3Sn on R-Al_2O_3 substrate (fig. S3).

It has been shown previously that hexagonal Mn_3Sn is stable with excess Mn. Specifically, earlier work on bulk $Mn_{3+x}Sn_{1-x}$ found that a maximum Mn excess of $x = 0.2$ could be achieved (*22*, *23*, *33*). The extra Mn atoms replace Sn atoms and randomly occupy the Sn sites (i.e., $Mn_{3+x}Sn_{1-x}$, $x > 0$). The replacement of nonmagnetic Sn atoms with magnetic atoms is expected to alter real space spin ordering and affect the spacing of Weyl nodes in the system. Density functional theory (DFT) calculations also suggest that extra Mn may raise the Fermi energy E_F (*22*). Therefore, doping with Mn should be an effective way to tune band structure topology and the Hall effects in $Mn_{3+x}Sn_{1-x}$.

As shown in the inset of Fig. 2A, for two distinct *x* values, the (0002) XRD peaks are well separated, indicating distinct values of lattice constant *c*. The lattice constant *a* is obtained from the $(20\bar{2}1)$ peak at tilted geometry via the relation of $a = 4c\,d_{(20\bar{2}1)}/\sqrt{3(c^2 - d^2_{(20\bar{2}1)})}$. As shown in Fig. 2D, lattice parameters *c* and *a* decrease as *x* increases, supporting replacement of Sn atoms by smaller Mn atoms. We found that the amount of Mn excess can be greatly extended to $x \approx 0.55$ in our epitaxial films without the introduction of an impurity phase. This result sharply contrasts the small compositional window seen in bulk samples and is likely related to the nonequilibrium growth conditions that exist during vacuum deposition processes. As *x* increases from 0.06 to 0.55, the *c* axis lattice constant decreases from 4.57 to 4.53 Å. Similar dependence of lattice parameters as a function of *x* is observed in (0001) $Mn_{3+x}Sn_{1-x}$ grown on Ag(111) seed layer on Si(111) wafer (Fig. 2D). The lattice parameters of $(11\bar{2}0)$ $Mn_{3+x}Sn_{1-x}$ show different dependence on *x*, but the unit cell volume still decreases as *x* increases (fig. S3). The greatly extended compositional range for replacing Sn with magnetic Mn in thin films allows for the exploration of new and unusual physics in Mn_3Sn, as exemplified below.

Kondo effect and gap opening by extended Mn doping

Figure 3A shows normalized resistance $\gamma(T)$ $[=R(T)/R(295\ \mathrm{K})]$ as a function of temperature (*T*) for 60-nm (0001) $Mn_{3+x}Sn_{1-x}$ films. Strictly speaking, a rigorous identification of metallicity requires demonstration that resistance extrapolates to a finite value at zero temperature, which is possible even if *R* is increasing as *T* decreases throughout the measurement range (*34*). For simplicity, here, we adopt the popular nomenclature that $\gamma(T)$ curves have a "metallic" ("insulating") characteristic if resistance decreases (increases) as *T* decreases. For reference, we note that bulk $Mn_{3+x}Sn_{1-x}$ ($x < 0.15$) single crystals show metallic behaviors with carrier density *n* about 2×10^{22} cm^{-3}. The resistivity of such bulk crystals is about 250 μΩ·cm at room temperature along the *ab* plane, indicating a mean-free path on the order of 1 nm (*35*). Broadly speaking, the $\gamma(T)$ character of our films is metallic for compositions below $x \sim 0.40$ and insulates above. For $x = 0.06$, γ decreases nearly linearly from room temperature to $T = 50$ K and reaches a residue value of about 0.76 at $T = 5$ K. As *x* increases to 0.11, metallic behavior remains, but with a larger γ at 5 K, consistent with the elevated scattering from Mn dopants randomly replacing the centers of the hexagons in the Kagome plane. Note that the transport contributions from the buffer and capping layers are minimized by using highly resistive materials (Materials and Methods).

The strong correlation among Mn *3d* electrons (*22*) in Mn_3Sn and its topological band structure suggest that Mn_3Sn is an ideal platform to explore the interplay between Weyl and correlation physics. In this material, Mn moments in the Kagome lattice are strongly antiferromagnetically coupled to each other, leading to various spin orders such as a planar 120° spin orientation with negligibly small net magnetization (*25*). The substituting Mn_{Sn} atom sitting at the hexagon center of the Kagome lattice could interact with its six neighbors via the Heisenberg exchange. However, the vanishing of total magnetic moment of the six neighbors results in the same energy no matter what direction the center spin points toward, to lowest order. Therefore, substitutional Mn spins may behave as magnetic impurities exchange coupled to the *d*-like conduction band states on the Mn-Kagome sublattice, leading to Kondo physics if the correlation is considerable. In the metallic regime, for example, the $x = 0.27$ film Fig. 3B shows a resistance upturn instead of a residue below the resistance minimum temperature $T_m = 25$ K. The $-\ln T$ increase in resistance with decreasing temperature at $T < T_m$ and the deviation of $\ln T$ scaling at lower temperature are characteristics of the Kondo effect (*36*). For simplicity, we adopt the deviation point of $\ln T$ scaling (Fig. 3B) as an estimation of the Kondo temperature T_K, which reflects the strength of Kondo interaction (*36*). The resistance increases as a result of Kondo scattering of magnetic impurities. As temperature further decreases, the Kondo scattering is inhibited because of the formation of a singlet state between a localized Mn moment and a conduction electron, which screens the magnetic moments of the impurities (*37*).

As *x* increases further and more Sn atoms are replaced by Mn atoms, T_m and T_K shift gradually to higher temperatures, indicating a stronger Kondo effect. For $x = 0.39$, T_m (T_K) is 47 K (23 K) (Fig. 3C). Above $x > 0.40$ (Fig. 3, D and E), the resistance shows an upturn at a much higher temperature (e.g., 192 K for $x = 0.44$, and >300 K for $x = 0.50$), consistent with the transition to a Kondo insulator as Kondo effect develops coherence in the dense Kondo lattice (*14*). The ground state of such a system features a hybridization gap, on the order of a few millielectron volts to tens of millielectron volts, near the Fermi energy (*14*, *15*), and because of the featured band inversion therein, most Kondo insulators are topologically nontrivial (*16*). A prominent example is the topological Kondo insulator SmB_6, which

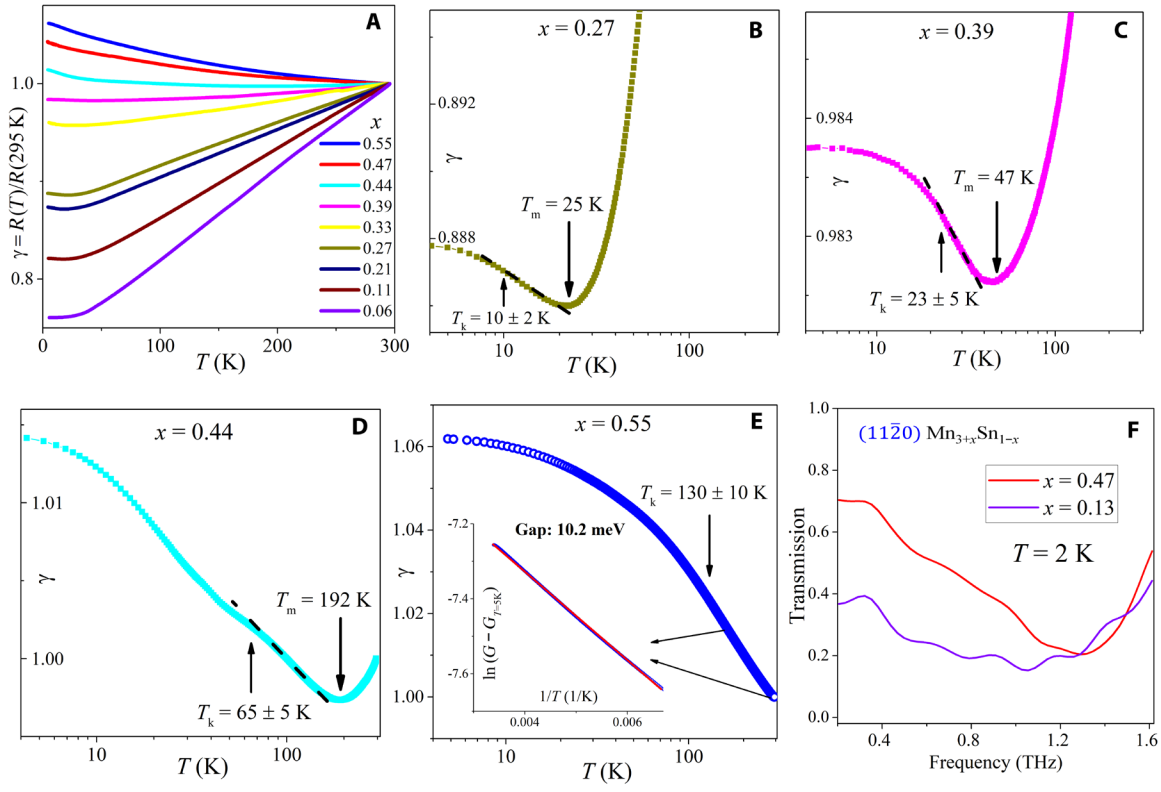

Fig. 3. Evolution of Kondo effect and gap opening in $Mn_{3+x}Sn_{1-x}$ films. Normalized resistance γ as a function of temperature for various x (**A**), for (**B**) $x = 0.27$, (**C**) $x = 0.39$, (**D**) $x = 0.44$, and (**E**) $x = 0.55$, respectively. Inset of (E): $\ln(G - G_{T=5K})$ as a function of $1/T$, and linear fit (red line) gives a gap value of 10.2 meV. (**F**) Transmission of $x = 0.47$ (red) and $x = 0.13$ (violet) samples as a function of frequency.

shows a small insulator gap of about 3 meV and a saturation resistance plateau at low temperatures (*38*). The $\gamma(T)$ curves of our highly doped films ($x > 0.40$) show a similar temperature dependence. As shown in Fig. 3E, for $x = 0.55$, the resistance exhibits a $-\ln T$ increase from room temperature to $T_K \sim 130$ K, then increases at a slower rate, and eventually reaches a near-saturated value at low temperature. Following the analysis in (*38*), we divide the measured conductance $G_{measured}$ into two parallel contributions: $G_{measured} = G_{T=5K} + G_{insulator}$, where $G_{T=5K}$ represents the near-saturated conductance at low temperature. $G_{T=5K}$ may originate from a topological surface state or an in-gap state (*39*). We plot $G_{insulator}$ as a function of $1/T$ from 300 to 150 K (inset of Fig. 3E). The linearity indicates that this analysis is appropriate and gives a gap value of 10.2 meV (i.e., 118 K $\approx T_K$), which corresponds well with reported gap values of other Kondo insulators (*15*). The gap opening at $x > 0.40$ is also evidenced by the decrease in carrier density as a function of temperature (fig. S4) due to reduced thermal activation at low temperature.

We briefly note that the Kondo effect and gap opening are also observed in thicker (0001) $Mn_{3+x}Sn_{1-x}$ films, as well as $(11\bar{2}0)$ oriented films, all with similar $\gamma(T)$ curves (fig. S4). Terahertz transmission measurements (Fig. 3F) at $T = 2$ K on a 60-nm $(11\bar{2}0)$ $Mn_{3+x}Sn_{1-x}$ ($x = 0.47$) show a prominent dip at 1.3 THz (~5.5 meV), which is less obvious in a metallic sample ($x = 0.13$). These terahertz transmission results echo the resistivity measurements and corroborate the notion of a gap opening. Even stronger evidence for the gap opening can be seen in terahertz Faraday rotation measurements discussed below.

Resonance-enhanced terahertz Faraday rotation

Here, we present a notable consequence of the gap opening in the terahertz Hall effect (i.e., Faraday rotation). Figure 4 shows the real (θ_F') and imaginary (θ_F'') parts of the Faraday rotation, which are related to each other by Kromers-Kronig transform. The metallic sample ($x = 0.13$) shows a small Faraday rotation on the order of a few milliradians (Fig. 4A), which is similar to the observed value in a recent study on polycrystalline Mn_3Sn films (*40*). In sharp contrast, for the gapped sample ($x = 0.47$), the imaginary part of the Faraday rotation, which is related to the ellipticity (θ_F''; Fig. 4B), shows a remarkable, resonance-enhanced peak at 1.33 THz (i.e., 5.6 meV, the aforementioned energy gap in the transmission measurements). According to the Kromers-Kronig relation, a resonance across the gap in the imaginary part corresponds to a sharp zero crossing (an inflection point) in the real part at 1.33 THz (Fig. 4A). We applied 6 T to align the magnetic domain first and then performed the Faraday rotation measurement by reducing the field from 4 to 0 T. The resonance-enhanced θ_F' is 0.3 rad at 4 T, which is around 40 times larger than that in the recent study on metallic Mn_3Sn films (*40*). The gap-induced resonance feature in optical rotations was also recently observed in a magnetic topological insulator (*41*). The resonance-enhanced terahertz Faraday rotation described here may represent an entirely new phenomenon in the world of the Kondo insulator, which was not observed in SmB_6 (*42*).

These above transport and terahertz results demonstrate a gap opening of WSM by doping of magnetic Mn atoms whose 3*d* electrons have strong correlations, and thus a possible transition from

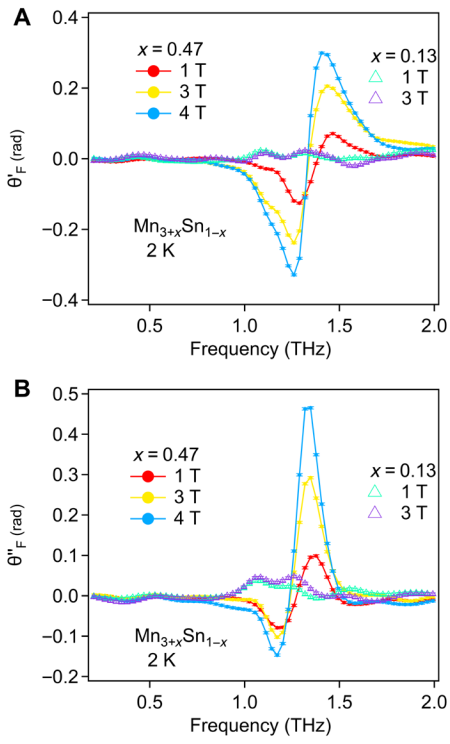

Fig. 4. Resonance-enhanced terahertz Faraday rotation in (11$\bar{2}$0) $Mn_{3+x}Sn_{1-x}$ films. Real part (**A**) and imaginary part (**B**) of the Faraday rotation as a function of frequency at different fields for $x = 0.47$ and $x = 0.13$ at $T = 2$ K.

Kondo effect to Kondo insulator in new class of topological matter. These effects are independent of the crystalline growth orientation.

DC Hall resistances arising from Berry curvatures in reciprocal and real spaces

One of the most salient transport features in bulk Mn_3Sn is the large spontaneous anomalous Hall resistance (AHR), arising from the Berry curvatures of the Weyl nodes (*22*, *25*). Therefore, the Weyl nature of our $Mn_{3+x}Sn_{1-x}$ thin film can be checked by Hall measurements. The total Hall resistivity includes various contributions and can be described as $\rho_H = R_0 B + R_S \mu_0 M + \rho_H^{AF}$, where M is the magnetization, R_0 (R_S) is the ordinary (anomalous) Hall coefficient (both R_0 and R_S are positive), and μ_0 is the magnetic permeability. Unlike conventional ferromagnets such as Fe and Co, where the Hall resistances only include the first two terms, there is an additional term ρ_H^{AF}, which is almost independent of B or M (*25*). Because usual antiferromagnets do not exhibit measurable spontaneous Hall resistances, ρ_H^{AF} presumably originates from the Berry curvatures in reciprocal or real space. The former contributes to an intrinsic anomalous Hall effect determined by the separation of Weyl nodes, while the latter manifests itself in topological Hall effect, as seen in chiral magnets (*43*) and oxide heterostructures (*44*). It is important to note that the exchange bias in $Mn_{3+x}Sn_{1-x}$/Py bilayers is observed at $T = 5$ K (fig. S5) in both metallic and gapped states. This is strong evidence that antiferromagnetism in our $Mn_{3+x}Sn_{1-x}$ films is robust over the whole compositional range we studied. Above the saturation field of the uncompensated spins (but below the spin-flop transition), $M = M_S^0 + \chi B/\mu_0$, where χ is the susceptibility and M_S^0 is the residual magnetization by extrapolating the high field M to $B = 0$. Therefore, above the saturation field, $\rho_H = (R_0 + \chi R_S) B + (R_S \mu_0 M_S^0 + \rho_H^{AF}) \equiv R_0^* B + \rho_{AHR}^*$, which includes a field-linear term and a field-independent term. In our films, independent of orientations, M_S^0 is on the order of 0.001 to 0.03 μ_B/Mn at room temperature, close to the resolution limit of the magnetometers used in this work (fig. S6 and note S2). In the following, we use bulk value $\chi \sim 3 \times 10^{-3}$ for our estimations (note S1).

We first consider the Hall effect in (11$\bar{2}$0) films for metallic states ($x < 0.4$). Figure S7A shows Hall resistance as a function of field for $Mn_{3+x}Sn_{1-x}$ ($x = 0.18$) at $T = 300$ K. The Hall loops indicate $-\rho_H^{AF} \approx -\rho_{AHR}^* \gg R_S \mu_0 M_S^0$ (fig. S7). The saturated Hall resistivity (ρ_{AHR}^*) at positive fields (e.g., $B = 9$ T) is negative. The negative AHR is a signature of the intrinsic contribution of Berry curvature in k-space, as observed in bulk single-crystal samples (*25*). Figure 5A shows the ρ_{AHR}^* ($\approx \rho_H^{AF}$) as a function of temperature for (11$\bar{2}$0) films with different x. For $x = 0.10$ and 0.18, ρ_{AHR}^* is as high as −1.5 μΩ·cm at 300 K. As temperature decreases, $|\rho_{AHR}^*|$ decreases and a clear transition around 225 K is observed. The transition at $T_1 \approx 225$ K, which is also observed in bulk Mn_3Sn single crystals (*35*), indicates changes from triangular spin order at higher temperatures to spin glass or spin spiral at low temperatures. Between $T_N = 420$ K and T_1, a WSM state exists because of the magnetic symmetry of triangular spin order (*22*). Below T_1, the intrinsic negative AHR decreases drastically due possibly to the disappearance of Weyl nodes in spin glass/spinal state. The ρ_H ($T < T_1$) is only about −0.2 μΩ·cm and depends weakly on temperature. At $x = 0.26$, where Kondo physics manifests at low temperature (Fig. 3B and fig. S4), a similar temperature dependence of ρ_{AHR}^* is observed; ρ_{AHR}^* remains negative at the whole temperature range despite slightly smaller values compared with those in films with $x = 0.10$ and 0.18.

However, at $x > 0.40$, the gapped state is realized, and ρ_{AHR}^* shows drastically different temperature dependence. At $T = 300$ K, ρ_{AHR}^* is only around −0.2 μΩ·cm, nearly an order-of-magnitude smaller than that of films with $x = 0.10$. This may be a direct consequence of a gap opening, which likely annihilates Weyl nodes and greatly reduces the Berry curvature. Alternatively, extended doping could also disrupt the triangular spin texture, which protects the Weyl nodes. ρ_{AHR}^* changes sign around T_1 (Fig. 5A). With extended doping ($x > 0.40$), the doped localized Mn moments start to form a lattice and disrupt the spin glass/spiral state at $T < T_1$. The doped Mn spins, along with Mn spins in the Kagome sites, are likely lying in the Kagome plane that is perpendicular to the film. These spins are "polarized" by the out-of-plane field (in the Kagome plane) and give rise to positive conventional AHR $R_S \mu_0 M_S^0 \left(\leq \rho_{AHR}^*$; note S3). Note that a positive ρ_H^{AF} may also contribute due to spin chirality if spins tilt toward the film plane.

ρ_{AHR}^* in (11$\bar{2}$0) $Mn_{3+x}Sn_{1-x}$ films are summarized in a T-x phase diagram shown in Fig. 5B. Large negative Hall resistance presumably induced by Weyl nodes exists at $T > 225$ K and $x < 0.40$. Notably, driven by the Kondo effect with higher Mn doping, a gapped state (possibly a Kondo insulator) emerges at $x > 0.40$ and shows positive Hall resistance at $T < 225$ K. These results indicate that magnetic doping is an effective way to tune electron correlations and Berry curvatures in the reciprocal space.

Although Kondo physics is similar in (0001) films, the Hall resistance shows different compositional dependence therein because of the anisotropy of the Hall effect in these materials. In bulk single crystals ($x < 0.15$), the M_S^0 and ρ_H^{AF} (ρ_{AHR}^*) are zero in the spin triangular state if the magnetic field is applied along the [0001] direction

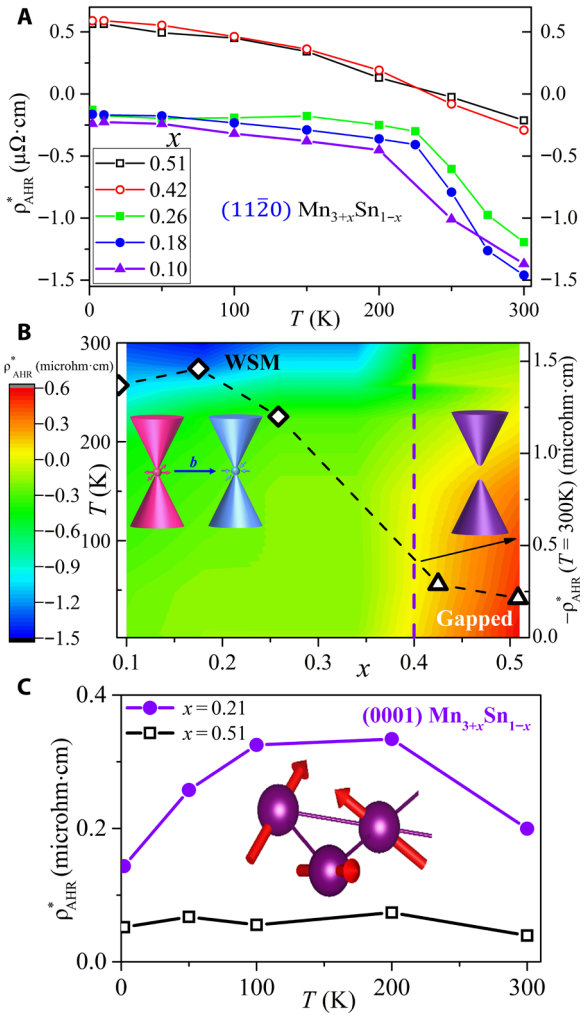

Fig. 5. Anomalous Hall effects and phase diagram of $Mn_{3+x}Sn_{1-x}$ films. (**A**) Anomalous Hall resistivity ρ^*_{AHR} as a function of temperature for different compositions for (11$\bar{2}$0) films. (**B**) Colored contour map of ρ^*_{AHR} in the *T*-*x* plane for (11$\bar{2}$0) films. Right *y* axis: $-\rho^*_{AHR}$ (*T* = 300 K) as a function of *x*. Inset of (B): Schematic diagrams of Weyl cones with opposite chirality and gapped cone. (**C**) Anomalous Hall resistivity ρ^*_{AHR} of (0001) films as a function of temperature for *x* = 0.21 (solid circles) and *x* = 0.51 (open squares), respectively.

(*25*). In the spin glass state, ρ^*_{AHR} is reported to be positive (*25*). In (0001) $Mn_{3+x}Sn_{1-x}$ films, a positive ρ^*_{AHR} is observed from 300 to 2 K. The ρ^*_{AHR} of the gapped state ($x > 0.40$; Fig. 5C and fig. S8) is much smaller than that of the metallic state. ρ^*_{AHR} of (0001) films in metallic state is substantially larger than the estimated upper limit of $R_S \mu_0 M_S^0$, indicating that ρ_H^{AF} is dominating (note S3). Furthermore, the major (9 T) and minor (1 T) Hall loops show distinct hysteresis (fig. S4A), in sharp contrast to the loops in (11$\bar{2}$0) films (fig. S7A). The intrinsic ρ_H^{AF} in (0001) films is likely field-induced topological Hall resistance (ρ^{TH}) (*45*), arising from the spin chirality in the real space (*27*). Considering a triangle spin structure shown in Fig. 5C, tilting of spins ($\boldsymbol{S}_i$, i = 1,2,3) toward the *c* axis gives a scalar spin chirality $\boldsymbol{S}_1 \cdot (\boldsymbol{S}_2 \times \boldsymbol{S}_3)$ (*27*), which induces a spin Berry phase (magnetic flux) $\Phi = 2r\Phi_0$, where Φ_0 is the flux quantum (2000 T·nm^2), and *r* reflects the fraction of the flux quantum (*r* is 1 for a magnetic skyrmion). The spin Berry phase gives rise a fictitious field $B_{eff} = \Phi/A = r \times 1.18 \times 10^5$ T, where $A = 0.034$ nm^2 is the area of each triangle. Therefore, a tiny value of *r* (note S3) can generate large B_{eff} that induces a topological Hall resistivity $\rho^{TH} = R_0 B_{eff}$ (e.g., ρ^{TH}=0.33 μΩ·cm for 60-nm films). In thicker films such as 120 nm with lower crystalline quality, tilting can easily take place, resulting in a larger *r*. The larger *r* thus corresponds to a larger ρ^{TH}, as echoed in the experiment (fig. S8). In contrast with ρ_H^{AF} in (11$\bar{2}$0) films, ρ^{TH} increases from $T = 300$ K to $T \approx T_1$ (225 K), but decreases noticeably at $T < 100$ K, which suggests a spin glass transition at $T_g \sim 100$ K (note S1). As mentioned above, for gapped states ($x > 0.40$), nearly half of hexagon centers are occupied by magnetic Mn atoms with spins randomly orienting in the Kagome plane. These doped (random) spins contribute to the spin chirality $[\boldsymbol{S}_1 \cdot (\boldsymbol{S}_2 \times \boldsymbol{S}_3)]$ with opposite signs so that the net spin chirality is (nearly) zero. These unusual Hall resistances in (11$\bar{2}$0) and (0001) films indicate that doping of magnetic Mn atoms is an effective knob to tune Berry curvatures in both real and reciprocal spaces.

Unusual magnetoresistance

Another important transport feature in WSMs is their negative magnetoresistance (NMR) due to the chiral anomaly. When a magnetic field is applied along the current direction, a chiral charge current is driven from one Weyl node to its counterpart with opposite chirality (*6*). This chiral current leads to additional electric conductivity and gives rise to NMR. The NMR effect is largest when $\boldsymbol{B} \parallel \boldsymbol{I}$ and vanishes when $\boldsymbol{B} \perp \boldsymbol{I}$ (*6*, *22*). The NMR effect has been observed in bulk Mn_3Sn single crystals, where it is very small (~0.1% at $B = 9$ T and $T = 300$ K) (*22*). Moreover, the NMR decreases quickly as the energy difference (ΔE) between Fermi energy and Weyl nodes increases. NMR is inversely proportional to ΔE^2 and is reduced by ~60% as ΔE increases from 5 meV ($x = 0.06$) to 8 meV ($x = 0.03$) (*22*). As shown in Fig. 6A and fig. S9A, a small ordinary positive magnetoresistance (PMR) due to Lorentz force is observed from $T = 300$ K to $T = 2$ K in our films for $x < 0.40$. The absence of NMR is likely due to the larger ΔE in those films. For the gapped state (Fig. 6B and fig. S9B), PMR is observed at $T > 70$ K, but NMR is observed at $T < 70$ K inside the spin glass regime (i.e., $T_g \sim 70$ K). The nearly linear NMR at low temperatures weakly depends on the orientation of the applied magnetic field. This isotropic NMR can originate from the suppressed Kondo scattering and/or spin-dependent scattering as magnetic field polarizes the randomly oriented doped Mn spins at the center of the hexagon (note S4). Nevertheless, the NMR well correlates with the $\gamma(T)$ and Hall results induced by Mn doping, providing complementary transport consequences by the magnetic doping of Mn atoms.

DISCUSSION

In this work, we show that AFM WSM $Mn_{3+x}Sn_{1-x}$ thin films with superior sample quality are a class of exciting materials to study the interplay between strong correlation, topology, and magnetism. By replacing Sn with magnetic Mn atoms, a Kondo effect, which often appears in strongly correlated metals, emerges, evolves, and leads to opening of a hybridization gap. As a consequence, Hall resistances inherent to Berry curvatures in the reciprocal space decreases. Notably, resonance-enhanced terahertz Faraday rotation emerges as the gap is opened. Our work calls for further studies of related materials. For example, one may increase electron localization (hence electron correlations) by doping atoms with 3*d* (e.g., Fe, Co, and Cu) or 5*f*/4*f*

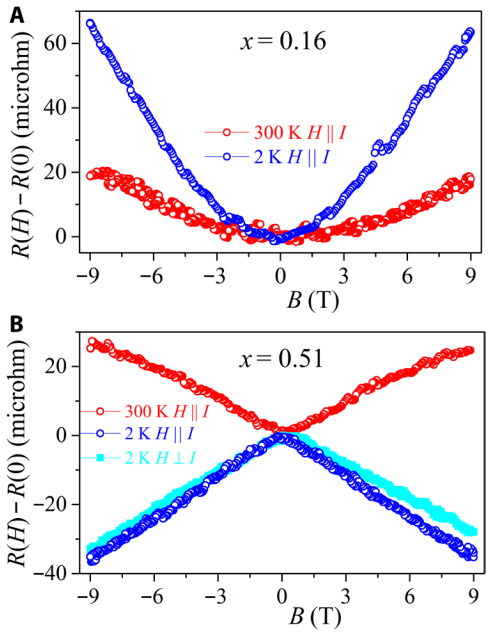

Fig. 6. Magnetoresistances of (0001) $Mn_{3+x}Sn_{1-x}$ films. Resistance change [$R(H) - R(H = 0)$] as a function of field for (**A**) $x = 0.16$ and (**B**) $x = 0.51$ at $T = 2$ K (blue) and $T = 300$ K (red).

(e.g., Gd) electrons (*14*). It is also interesting to tune the spin-orbit coupling by doping (especially isostructural and/or isoelectronic doping) of heavy elements (e.g., Pb).

One of the major challenges in AFM spintronics is the electric detection of AFM spin order. In this respect, conventional collinear AFMs, which do not exhibit AHRs due to vanishingly small magnetization, are not good candidates for AFM spintronics (*28*). The rich noncollinear spin textures and the substantial Hall resistances in the Mn_3Sn family of compounds make it a promising contender for such applications. Moreover, the noncollinear spin orders and/or the topological aspects in Mn_3Sn present new opportunities for spin-charge conversion and spin orbit torque switching of AFM spin orders. These $Mn_{3+x}Sn_{1-x}$ films with greatly extended compositional range, tunable strong correlations, unusual Hall resistances, and resonance-enhanced terahertz Faraday rotation, offer new prospects, as exemplified in this work, and may further propel the nascent field of topological AFM/terahertz spintronics and the development of novel spin-based devices.

MATERIALS AND METHODS

The $Mn_{3+x}Sn_{1-x}$ films were synthesized by DC cosputtering of Mn (99.99%) and Sn (99.99%) targets at a sputtering rate of about 2 Å/s in a high-vacuum magnetron sputtering system with base pressure better than 5×10^{-8} torr. Each batch of films with compositional wedge (pure phase) was grown on a wafer with dimensions approximately 7 mm by 50 mm. After growth, the wafer was cut into 13 to 14 pieces (each of them had a size of around 3.5 mm by 7 mm) along the wedge direction for XRD measurements. Each piece was further cut for transport (~2 mm by 3.5 mm; electrodes were made by wire bonder) and/or other characterizations. (0001) $Mn_{3+x}Sn_{1-x}$ films were grown at substrate temperature of $T_S \approx 300$°C on C-Al_2O_3 substrate with Pt seed layer and Si (111) substrate with Ag seed layer. ($11\bar{2}0$) $Mn_{3+x}Sn_{1-x}$ films were grown at substrate temperature of $T_S \approx 400$°C on R-Al_2O_3 substrate without seed layer. The samples presented in this work are listed in table S1. The compositions of films were measured/calibrated on 150-nm (0001) $Mn_{3+x}Sn_{1-x}$ films by energy-dispersive spectroscopy (EDS) in a scanning electron microscope. For transport measurements on (0001) films, the buffer layer (Pt) is slightly doped (or the thickness is reduced) to increase the resistivity but retains its crystalline quality, so that the contribution from the buffer layer is minimized. The magnetization measurements were done in a Quantum Design PPMS system equipped with a vibrating sampling magnetometer (VSM) and a room temperature VSM. The DC transport measurements were done in a 9-T cryogen-free Quantum Design PPMS system with transport rotator assembly. Terahertz measurements were done in a home-built spectrometer that is coupled to a cryogen-free 7-T split-coil superconducting magnet with a base temperature of 1.6 K.

SUPPLEMENTARY MATERIALS

Supplementary material for this article is available at http://advances.sciencemag.org/cgi/content/full/6/35/eabc1977/DC1

REFERENCES AND NOTES

1. K. v. Klitzing, G. Dorda, M. Pepper, New method for high-accuracy determination of the fine-structure constant based on quantized Hall resistance. *Phys. Rev. Lett.* **45**, 494–497 (1980).
2. K. S. Novoselov, A. K. Geim, S. V. Morozov, D. Jiang, Y. Zhang, S. V. Dubonos, I. V. Grigorieva, A. A. Firsov, Electric field effect in atomically thin carbon films. *Science* **306**, 666–669 (2004).
3. C. L. Kane, E. J. Mele, Z_2 topological order and the quantum spin Hall effect. *Phys. Rev. Lett.* **95**, 146802 (2005).
4. A. A. Burkov, L. Balents, Weyl semimetal in a topological insulator multilayer. *Phys. Rev. Lett.* **107**, 127205 (2011).
5. X. Wan, A. M. Turner, A. Vishwanath, S. Y. Savrasov, Topological semimetal and Fermi-arc surface states in the electronic structure of pyrochlore iridates. *Phys. Rev. B* **83**, 205101 (2011).
6. N. P. Armitage, E. J. Mele, A. Vishwanath, Weyl and Dirac semimetals in three-dimensional solids. *Rev. Mod. Phys.* **90**, 015001 (2018).
7. A. A. Zyuzin, A. A. Burkov, Topological response in Weyl semimetals and the chiral anomaly. *Phys. Rev. B* **86**, 115133 (2012).
8. K.-Y. Yang, Y.-M. Lu, Y. Ran, Quantum Hall effects in a Weyl semimetal: Possible application in pyrochlore iridates. *Phys. Rev. B* **84**, 075129 (2011).
9. C. Y. Guo, F. Wu, Z. Z. Wu, M. Smidman, C. Cao, A. Bostwick, C. Jozwiak, E. Rotenberg, Y. Liu, F. Steglich, H. Q. Yuan, Evidence for Weyl fermions in a canonical heavy-fermion semimetal YbPtBi. *Nat. Commun.* **9**, 4622 (2018).
10. Y. Xu, J. Zhao, C. Yi, Q. Wang, Q. Yin, Y. Wang, X. Hu, L. Wang, E. Liu, G. Xu, L. Lu, A. A. Soluyanov, H. Lei, Y. Shi, J. Luo, Z.-G. Chen, Electronic correlations and flattened band in magnetic Weyl semimetal $Co_3Sn_2S_2$. arXiv: 1908.04561, (2019).
11. V. Ivanov, X. Wan, S. Y. Savrasov, Topological insulator-to-Weyl semimetal transition in strongly correlated actinide system UNiSn. *Phys. Rev. X* **9**, 041055 (2019).
12. Y. Shao, A. N. Rudenko, J. Hu, Z. Sun, Y. Zhu, S. Moon, A. J. Millis, S. Yuan, A. I. Lichtenstein, D. Smirnov, Z. Q. Mao, M. I. Katsnelson, D. N. Basov, Electronic correlations in nodal-line semimetals. *Nat. Phys.* **16**, 636–641 (2020).
13. J. Kondo, Resistance minimum in dilute magnetic alloys. *Prog. Theor. Phys.* **32**, 37–49 (1964).
14. P. Coleman, Heavy Fermions and the Kondo Lattice: A 21st Century Perspective. arXiv: 1509.05769, (2015).
15. Z. Fisk, J. L. Sarrao, J. D. Thompson, D. Mandrus, M. F. Hundley, A. Miglori, B. Bucher, Z. Schlesinger, G. Aeppli, E. Bucher, J. F. Di Tusa, C. S. Oglesby, H.-R. Ott, P. C. Canfield, S. E. Brown, Kondo insulators. *Physica B* **206-207**, 798–803 (1995).
16. M. Dzero, J. Xia, V. Galitski, P. Coleman, Topological Kondo insulators. *Annu. Rev. Condens. Matter Phys.* **7**, 249–280 (2016).
17. D. Ma, H. Chen, H. Liu, X. C. Xie, Kondo effect with Weyl semimetal Fermi arcs. *Phys. Rev. B* **97**, 045148 (2018).
18. A. K. Mitchell, L. Fritz, Kondo effect in three-dimensional Dirac and Weyl systems. *Phys. Rev. B* **92**, 121109 (2015).
19. A. Principi, G. Vignale, E. Rossi, Kondo effect and non-Fermi-liquid behavior in Dirac and Weyl semimetals. *Phys. Rev. B* **92**, 041107 (2015).

20. H.-H. Lai, S. E. Grefe, S. Paschen, Q. Si, Weyl-Kondo semimetal in heavy-fermion systems. *Proc. Natl. Acad. Sci. U.S.A.* **115**, 93–97 (2018).
21. S. Dzsaber, X. Yan, M. Taupin, G. Eguchi, A. Prokofiev, T. Shiroka, P. Blaha, O. Rubel, S. E. Grefe, H.-H. Lai, Q. Si, S. Paschen, Giant spontaneous Hall effect in a nonmagnetic Weyl-Kondo semimetal. arXiv: 1811.02819, (2018).
22. K. Kuroda, T. Tomita, M.-T. Suzuki, C. Bareille, A. A. Nugroho, P. Goswami, M. Ochi, M. Ikhlas, M. Nakayama, S. Akebi, R. Noguchi, R. Ishii, N. Inami, K. Ono, H. Kumigashira, A. Varykhalov, T. Muro, T. Koretsune, R. Arita, S. Shin, T. Kondo, S. Nakatsuji, Evidence for magnetic Weyl fermions in a correlated metal. *Nat. Mater.* **16**, 1090–1095 (2017).
23. M. Ikhlas, T. Tomita, T. Koretsune, M.-T. Suzuki, D. Nishio-Hamane, R. Arita, Y. Otani, S. Nakatsuji, Large anomalous Nernst effect at room temperature in a chiral antiferromagnet. *Nat. Phys.* **13**, 1085–1090 (2017).
24. M. Kimata, H. Chen, K. Kondou, S. Sugimoto, P. K. Muduli, M. Ikhlas, Y. Omori, T. Tomita, A. H. MacDonald, S. Nakatsuji, Y. Otani, Magnetic and magnetic inverse spin Hall effects in a non-collinear antiferromagnet. *Nature* **565**, 627–630 (2019).
25. S. Nakatsuji, N. Kiyohara, T. Higo, Large anomalous Hall effect in a non-collinear antiferromagnet at room temperature. *Nature* **527**, 212–215 (2015).
26. N. H. Sung, F. Ronning, J. D. Thompson, E. D. Bauer, Magnetic phase dependence of the anomalous Hall effect in Mn_3Sn single crystals. *Appl. Phys. Lett.* **112**, 132406 (2018).
27. H. Ishizuka, N. Nagaosa, Spin chirality induced skew scattering and anomalous Hall effect in chiral magnets. *Sci. Adv.* **4**, eaap9962 (2018).
28. T. Jungwirth, J. Sinova, A. Manchon, X. Marti, J. Wunderlich, C. Felser, The multiple directions of antiferromagnetic spintronics. *Nat. Phys.* **14**, 200–203 (2018).
29. L. Šmejkal, Y. Mokrousov, B. Yan, A. H. MacDonald, Topological antiferromagnetic spintronics. *Nat. Phys.* **14**, 242–251 (2018).
30. A. Markou, J. M. Taylor, A. Kalache, P. Werner, S. S. P. Parkin, C. Felser, Noncollinear antiferromagnetic Mn_3Sn films. *Phys. Rev. Mater.* **2**, 051001 (2018).
31. Y. You, X. Chen, X. Zhou, Y. Gu, R. Zhang, F. Pan, C. Song, Anomalous Hall effect–like behavior with in-plane magnetic field in noncollinear antiferromagnetic Mn_3Sn Films. *Adv. Electron. Mater.* **5**, 1800818 (2019).
32. T. Higo, D. Qu, Y. Li, C. L. Chien, Y. Otani, S. Nakatsuji, Anomalous Hall effect in thin films of the Weyl antiferromagnet Mn_3Sn. *Appl. Phys. Lett.* **113**, 202402 (2018).
33. P. J. Brown, V. Nunez, F. Tasset, J. B. Forsyth, P. Radhakrishna, Determination of the magnetic structure of Mn_3Sn using generalized neutron polarization analysis. *J. Phys. Condens. Matter* **2**, 9409 (1990).
34. P. M. Vora, P. Gopu, M. Rosario-Canales, C. R. Pérez, Y. Gogotsi, J. J. Santiago-Avilés, J. M. Kikkawa, Correlating magnetotransport and diamagnetism of sp^2-bonded carbon networks through the metal-insulator transition. *Phys. Rev. B* **84**, 155114 (2011).
35. X. Li, L. Xu, L. Ding, J. Wang, M. Shen, X. Lu, Z. Zhu, K. Behnia, Anomalous Nernst and Righi-Leduc effects in Mn_3Sn: Berry curvature and entropy flow. *Phys. Rev. Lett.* **119**, 056601 (2017).
36. L. J. Zhu, S. H. Nie, P. Xiong, P. Schlottmann, J. H. Zhao, Orbital two-channel Kondo effect in epitaxial ferromagnetic $L1_0$-MnAl films. *Nat. Commun.* **7**, 10817 (2016).
37. H. Xue, Y. Hong, C. Li, J. Meng, Y. Li, K. Liu, M. Liu, W. Jiang, Z. Zhang, L. He, R. Dou, C. Xiong, J. Nie, Large negative magnetoresistance driven by enhanced weak localization and Kondo effect at the interface of $LaAlO_3$ and Fe-doped $SrTiO_3$. *Phys. Rev. B* **98**, 085305 (2018).
38. Y. Li, Q. Ma, S. X. Huang, C. L. Chien, Thin films of topological Kondo insulator candidate SmB_6: Strong spin-orbit torque without exclusive surface conduction. *Sci. Adv.* **4**, eaap8294 (2018).
39. Z. Xiang, Y. Kasahara, T. Asaba, B. Lawson, C. Tinsman, L. Chen, K. Sugimoto, S. Kawaguchi, Y. Sato, G. Li, S. Yao, Y. L. Chen, F. Iga, J. Singleton, Y. Matsuda, L. Li, Quantum oscillations of electrical resistivity in an insulator. *Science* **362**, 65–69 (2018).
40. T. Matsuda, N. Kanda, T. Higo, N. P. Armitage, S. Nakatsuji, R. Matsunaga, Room-temperature terahertz anomalous Hall effect in Weyl antiferromagnet Mn_3Sn thin films. *Nat. Commun.* **11**, 909 (2020).
41. S. Patankar, J. P. Hinton, J. Griesmar, J. Orenstein, J. S. Dodge, X. Kou, L. Pan, K. L. Wang, A. J. Bestwick, E. J. Fox, D. Goldhaber-Gordon, J. Wang, S.-C. Zhang, Resonant magneto-optic Kerr effect in the magnetic topological insulator Cr: $(Sb_xBi_{1-x})_2Te_3$. *Phys. Rev. B* **92**, 214440 (2015).
42. N. J. Laurita, C. M. Morris, S. M. Koohpayeh, P. F. S. Rosa, W. A. Phelan, Z. Fisk, T. M. McQueen, N. P. Armitage, Anomalous three-dimensional bulk ac conduction within the Kondo gap of SmB_6 single crystals. *Phys. Rev. B* **94**, 165154 (2016).
43. S. X. Huang, C. L. Chien, Extended skyrmion phase in epitaxial FeGe(111) thin films. *Phys. Rev. Lett.* **108**, 267201 (2012).
44. W. Wang, M. W. Daniels, Z. Liao, Y. Zhao, J. Wang, G. Koster, G. Rijnders, C.-Z. Chang, D. Xiao, W. Wu, Spin chirality fluctuation in two-dimensional ferromagnets with perpendicular magnetic anisotropy. *Nat. Mater.* **18**, 1054–1059 (2019).
45. P. K. Rout, P. V. P. Madduri, S. K. Manna, A. K. Nayak, Field-induced topological Hall effect in the noncoplanar triangular antiferromagnetic geometry of Mn_3Sn. *Phys. Rev. B* **99**, 094430 (2019).

Acknowledgments

Funding: X.H. and L.W. acknowledge support by the Amy Research Office under the grant W911NF1910342. The Penn NSF MRSEC DMR-1720530 supported part of the magneto-terahertz instrumentation development (L.W.) and the electrical transport measurements (S.H.P. and J.M.K.). J.Z. acknowledges the financial support by the U.S. Department of Energy (DOE), Office of Science, Basic Energy Sciences (BES) under award no. DE-SC0020221. J.W. acknowledges the support by the Department of Energy, Office of Science, Basic Energy Sciences, Materials Sciences and Engineering Division, under contract DE-AC02-76SF00515. R.F.N. acknowledges support from the National Research Council Research Associateship Program. Research was performed, in part, at the NIST Center for Nanoscale Science and Technology. P.K. and W.W. acknowledges support by the NSF under the grant DMR-1905783.

Author contributions: S.X.H. conceived the project. D.K. synthesized the films and performed the XRD measurements. T.R.T., S.H.P., and J.M.K. performed the DC transport measurements. X.H. and L.W. performed the terahertz measurements and analyzed the data. J.W., P.K., and W.W. performed magnetic measurements. R.F.N. did HR-XRD and EDS measurements. S.X.H. analyzed the data with assistance from T.R.T. and D.K. and inputs from all authors. S.X.H. and J.Z. discussed the results and gave explanations. S.X.H. wrote the manuscript, with revisions from J.Z., J.M.K., L.W., and R.F.N. and comments from all authors.
Competing interests: The authors declare that they have no competing interests. **Data and materials availability:** All data needed to evaluate the conclusions in the paper are present in the paper and/or the Supplementary Materials. Additional data related to this paper may be requested from the authors.

Submitted 10 April 2020
Accepted 16 July 2020
Published 28 August 2020
10.1126/sciadv.abc1977

Citation: D. Khadka, T. R. Thapaliya, S. Hurtado Parra, X. Han, J. Wen, R. F. Need, P. Khanal, W. Wang, J. Zang, J. M. Kikkawa, L. Wu, S. X. Huang, Kondo physics in antiferromagnetic Weyl semimetal $Mn_{3+x}Sn_{1-x}$ films. *Sci. Adv.* **6**, eabc1977 (2020).